Application of the reverberation waveform inversion for the high-resolution sediment layer structure in the Pacific

HyeJeong Kim [1,2] Hitoshi Kawakatsu [1,3] Takeshi Akuhara [1] Nozomu Takeuchi [1]
Takehi Isse,[1] Hajime Shiobara,[1] Hiroko Sugioka [4] Hisashi Utada,[1] YoungHee Kim [5]
and Sang-Mook Lee[5]

[1] *Earthquake Research Institute, University of Tokyo, Tokyo* 113-0032, *Japan. E-mails:* hkim.geo@gmail.com *(HJK);* takeuchi@eri.u-tokyo.ac.jp *(NT)*
[2] *Department of Geology and Geophysics, The University of Utah, Salt Lake City, UT* 84112, *USA*
[3] *Institute of Earth Sciences, Academia Sinica, Taipei* 11529, *Taiwan*
[4] *Department of Planetology, Graduate School of Science, Kobe University, Kobe, Hyogo* 657-8501, *Japan*
[5] *School of Earth and Environmental Sciences, Seoul National University, Seoul* 08826, *Republic of Korea*

SUMMARY

This study presents the velocity structures of the seafloor sediment across the Pacific using teleseismic body waves recorded by arrays of ocean bottom seismometers (OBSs). We apply the method inverting the multicomponent stacked autocorrelation functions and radial-component waveform of teleseismic body waves. We analyze OBSs distributed across the Pacific Ocean, through a wide range of water depths and equipped with various sensor types. The inverted models agreeing with measurements of seafloor drilling samples demonstrate the broad applicability of employing the inversion method to resolve sediment thicknesses ranging from <100 m to a few kilometers. In addition to various broad-band OBSs, we confirm our method works also for short-period sensors, since our retrieved the model using data from a short-period sensor in Northeast Japan agrees with active-source seismic survey analyses. The constrained models show various numbers of intrasediment discontinuities across different locations. Furthermore, the newly characterized sediment models have higher values of P-wave to S-wave velocity ratio (V_P/V_S) than the previously known scaling relationships, which suggests a larger effect of sediment-layer reverberation on the body-wave analysis than we have anticipated. The sediment velocity models obtained in this study produce Rayleigh-wave admittances that are consistent with those in previous studies but with much finer structural details within the sediment layer. The reverberation waveform inversion method will enable improved predictions of the impact of the water and sediment layers in body-wave records from existing and future OBS observations.

Key words: Pacific Ocean; Body waves; Crustal imaging; Waveform inversion.

1 INTRODUCTION

Ocean bottom seismometers (OBSs) have provided new opportunities for understanding the dynamics of the lithosphere–asthenosphere system and the mantle convection by enabling high-resolution seismic analysis of the Earth's interior. For example, high-resolution investigations of seismic attenuation (e.g. Takeuchi *et al.* 2017; Saikia *et al.* 2021; Russell & Dalton 2022), seismic anisotropy of the upper mantle (e.g. Eilon *et al.* 2014; Takeo *et al.* 2018; Takeuchi *et al.* 2023) and compressional-wave (*P*-wave) and shear-wave (*S*-wave) velocity anomalies in the mantle (e.g. Schlömer *et al.* 2017; Barruol *et al.* 2019; Eilon *et al.* 2022; Kang *et al.* 2023), have been conducted using *in situ* OBS data. Receiver function analyses have provided insights on

the existing melt layers in the lithosphere–asthenosphere system (e.g. Kawakatsu *et al.* 2009; Chen *et al.* 2024). New ocean bottom seismic deployments are constantly expanding the spatial coverage for such detailed seismic analyses (e.g. Pacific Array https://eri-ndc.eri.u-tokyo.ac.jp/PacificArray/; Kawakatsu & Utada 2017).

Along with the increase in studies utilizing OBS data, the importance of considering the water column and seafloor sediment layers in OBS-based seismic analyses has garnered considerable attention. Their significance has been particularly recognized and discussed for body-wave analyses, such as *P*- and *S*-receiver functions (e.g. Akuhara *et al.* 2021), and body-wave tomography (e.g. Obayashi *et al.* 2017). *In situ* sediment models are helpful for evaluating the potential contamination of observed OBS waveforms by
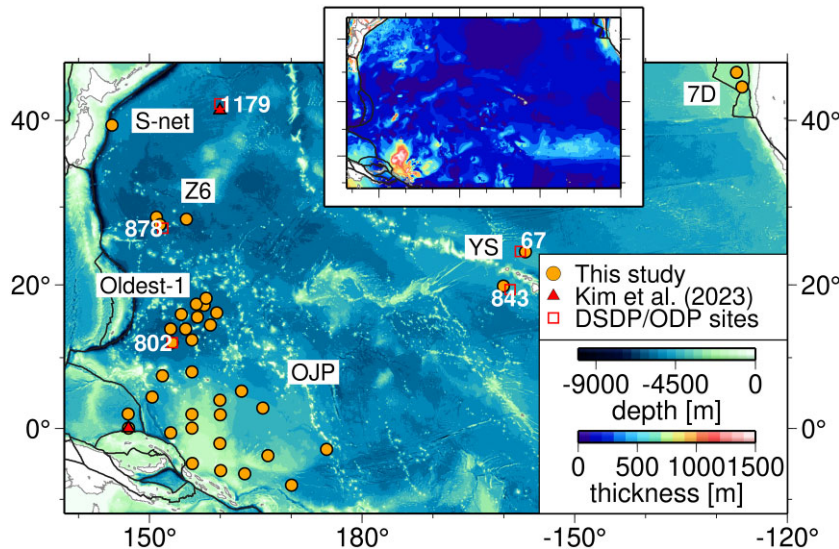
Figure 1. Map showing the targets of this study with the global topography in the background. The orange circles mark the locations of the OBSs, with the names of the OBS arrays provided in white boxes. The red triangles indicate the stations discussed by Kim *et al.* (2023). The red squares denote the Deep Sea Drilling Project (DSDP) and Ocean Drilling Program (ODP) locations, with their associated site numbers. The inlet map shows the global sediment thickness (Straume *et al.* 2019) in the same domain. The black lines mark tectonic plate boundaries. Further information on the OBS arrays is provided in Table S1 (Supporting Information).

the phases from low-velocity shallow layers (i.e. sediments, water). Various approaches to infer sediment models have been used (e.g. Hannemann *et al.* 2016; Chichester *et al.* 2020). Sediment models that explain the observations (e.g. traveltime through the sediment layer) are used to correct for expected contamination (e.g. Rychert *et al.* 2018); alternatively, the time delay and amplification from the sediment layer are corrected via an ad-hoc approach (e.g. Kim *et al.* 2021; Dai *et al.* 2023). An accurate model is therefore necessary to fully distinguish the contamination from the water and seafloor sediment layers in the waveforms.

The persistence of reflected and converted body waves from the sediment layer (i.e. reverberations) highly depends on the existence of sharp intrasediment velocity jumps and the ratio of *P*-wave velocity (V_P) to *S*-wave velocity (V_S) (V_P/V_S) in these layers. For example, a single-layer and multilayer sediment model may explain the same timing of the Ps (or Sp) converted phase from the sediment basement, even though they may have distinct waveforms at both low and high frequencies upon an incident *P* wave (or *S* wave) (Kim *et al.* 2023). Different sediment structures have distinct effects on the waveforms of the Sp and Ps phases that are converted at a mantle discontinuity (e.g. lithosphere–asthenosphere boundary, 410-km discontinuity). The degree of distortion that occurs in waveforms (timing and amplitude) of Sp/Ps phases converted at major discontinuities should be considered carefully using high-resolution V_P/V_S models.

A high-resolution velocity model of the seafloor sediment layer, which includes intrasediment discontinuities, might be obtained from an active-source seismic survey or laboratory measurements of samples from seafloor drilling. However, such surveys or direct measurements are not always available when analyzing OBS array observations. Furthermore, active-seismic source surveys and drilling core measurements are often limited to V_P measurements and therefore lack V_P/V_S information.

A novel method by Kim *et al.* (2023) utilizes the waveforms for the radial, vertical and pressure components of incident teleseismic body (*P* and *S*) waves to resolve intrasediment discontinuities

(hereafter referred to as 'reverberation waveform inversion'). While solving these parameters intrinsically suffers from parameter trade-offs, Kim *et al.* (2023) used multicomponent data to effectively mitigate such trade-offs; specifically, the *P*- and *S*-wave impedances, traveltimes, and V_P/V_S can be determined independently. Kim *et al.* (2023) demonstrated the agreement among parameters using the direct and active-source seismic measurements at an OBS station in the Northwest Pacific (Shinohara *et al.* 2008), as well as other measurements. However, whether the reverberation inversion works properly or not involves many factors, such as data quality (depending on instrument type, observation period, availability of pressure sensors, etc.) and the nature of sediment structures (the number of layers included, total thickness, etc.). In this context, to further demonstrate the effectiveness of the method, here we apply our approach to various types of OBSs from different regions of the Pacific and compare them with previous measurements and/or models. We also use the compiled sediment layer models and their V_P/V_S structures to discuss their implications for passive ocean-bottom seismology.

2 DATA: OCEAN BOTTOM SEISMOMETERS IN THE PACIFIC

We select multiple OBS arrays in the Pacific (Fig. 1; Table S1, Supporting Information) that have been deployed by various institutions and countries and consist of OBSs with different designs and sensor types. Furthermore, the OBSs from the selected arrays have been placed at various seafloor depths and distances from land. Therefore, we expect a wide range of seafloor sediment thicknesses below the selected OBSs (Fig. 1).

2.1 Stations from Japan (1): Oldest-1 array

We analyze 11 stations from the Oldest-1 array (Fig. 1; Kawano *et al.* 2023) that were deployed around 170 Ma seafloor in the western Pacific. The array consists of broad-band OBSs (BBOBSs)
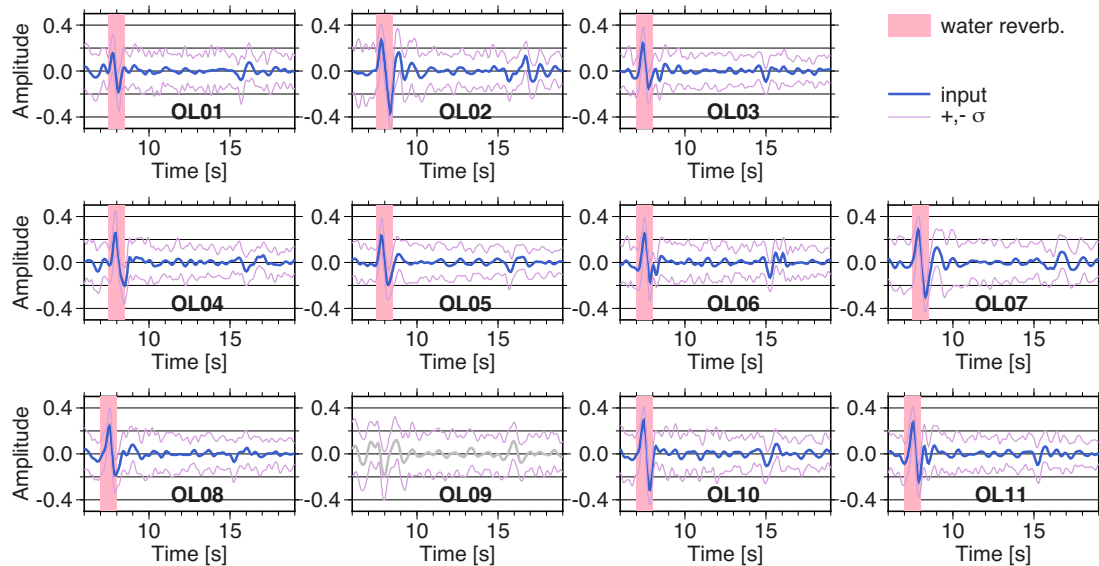
Figure 2. Stacked Z-ACFs of the teleseismic *P*-waves (blue) for the Oldest-1 array stations. The autocorrelation functions are calculated using the Gaussian low-pass parameter $a = 5.0$ and smoothing window width $W = 0.8$. The thin light-purple lines are $\pm 2\sigma$ from the stacked curves (thick blue), which are estimated from the standard deviation of the autocorrelation functions. Vertical pink shades mark the timing of the water reverberation phase. The associated P-ACF and R-ACF stacks are plotted in Figs S1 and S2 (Supporting Information), respectively. Station OL09 showed unexpected behavior in the vertical autocorrelation function (light-gray; see Fig. S3, Supporting Information) and was not used in the analysis.

with differential pressure gauges (DPGs) that operated from 2018 November to 2019 October as a Japan–South Korea research collaboration under the Pacific Array initiative (https://eri-ndc.eri.u-tokyo.ac.jp/PacificArray/; last accessed 2023 December 19). Recent studies using long-period body-wave traveltimes (Kang *et al.* 2023) and surface-wave dispersion array analysis (Kawano *et al.* 2023) have enhanced our understanding of the upper mantle dynamics beneath the 170 Ma Pacific seafloor, which is the oldest oceanic crust on Earth.

Global sediment models (e.g. Straume *et al.* 2019) expect a relatively thick sediment layer (400–1200 m) around the Oldest-1 array owing to the old age of the seafloor and surrounding Cretaceous volcanic activity (e.g. Koppers *et al.* 2003). Seafloor drilling in the region (Lancelot *et al.* 1990) has reported that the sediment layer is >500 m thick.

2.2 Stations from Japan (2): OJP array

The Ontong Java Plateau array (OJP array) is located to the south of the Oldest-1 array. They consist of BBOBSs and only some of the stations in this array are equipped with DPGs. The mantle beneath the Ontong Java Plateau has been studied via receiver function analysis (Tonegawa *et al.* 2019), *P*-wave tomography (Obayashi *et al.* 2021), and surface-wave tomography (Isse *et al.* 2021). The sediment structure beneath station OJ03 is discussed in detail by Kim *et al.* (2023).

2.3 Stations from US arrays

We selectively choose BBOBS arrays from US institutions (Table S1, Supporting Information) to demonstrate the wide applicability of the method in various environments. We choose stations from the Forsyth Deployment near the South Shatsky Fracture Zone (Z6;

2009–2010), Plume Lithosphere Undersea Melt Experiment (YS; 2004–2007) and Cascadia Initiative Community Experiment—OBS Component (7D; 2011–2017). Some of these selected stations are located close to Deep Sea Drilling Project (DSDP) or Ocean Drilling Project (ODP) sites (Fig. 1). Although the sediment layer thickness and/or velocities were not estimated at some DSDP/ODP sites (e.g. Site 878 in the Northwest Pacific), we compared the sediment properties within the available extent. The Z6 array lies across a region of thin sediment (<100 m; Straume *et al.* 2019) and was selected to demonstrate the resolvability of thin sediment layers using our method. For stations in the YS array, sediment properties have been estimated from drilling core samples and sediment structure has been constrained from seafloor compliance (Doran & Laske 2019). The 7D array was selected to compare our inversion results with those from Rayleigh-wave admittance and the radial component delay time due to the sediment layer (i.e. PS-P time) (Ruan *et al.* 2014; Bell *et al.* 2015).

2.4 Short period sensor: S-net

We also analyze one station from the real-time telemetered permanent ocean-bottom cable network (S-net; National Research Institute for Earth Science & Disaster Resilience 2019) in Japan. The S-net consists of short-period velocity meters that give reliable noise spectra above 0.2 Hz (Takagi *et al.* 2020). Station S6N09, which is located on the outer rise of the Japan Trench, has V_P and V_P/V_S constraints from active-source seismic surveys (Fujie *et al.* 2013; Nakamura *et al.* 2014) that indicate the presence of a sharp velocity jump within the sedimentary unit. Instrument response for the short-period sensor is not corrected since the autocorrelation function is normalized by the smoothed spectrum (Kim *et al.* 2023), which makes the data free from instrument response.
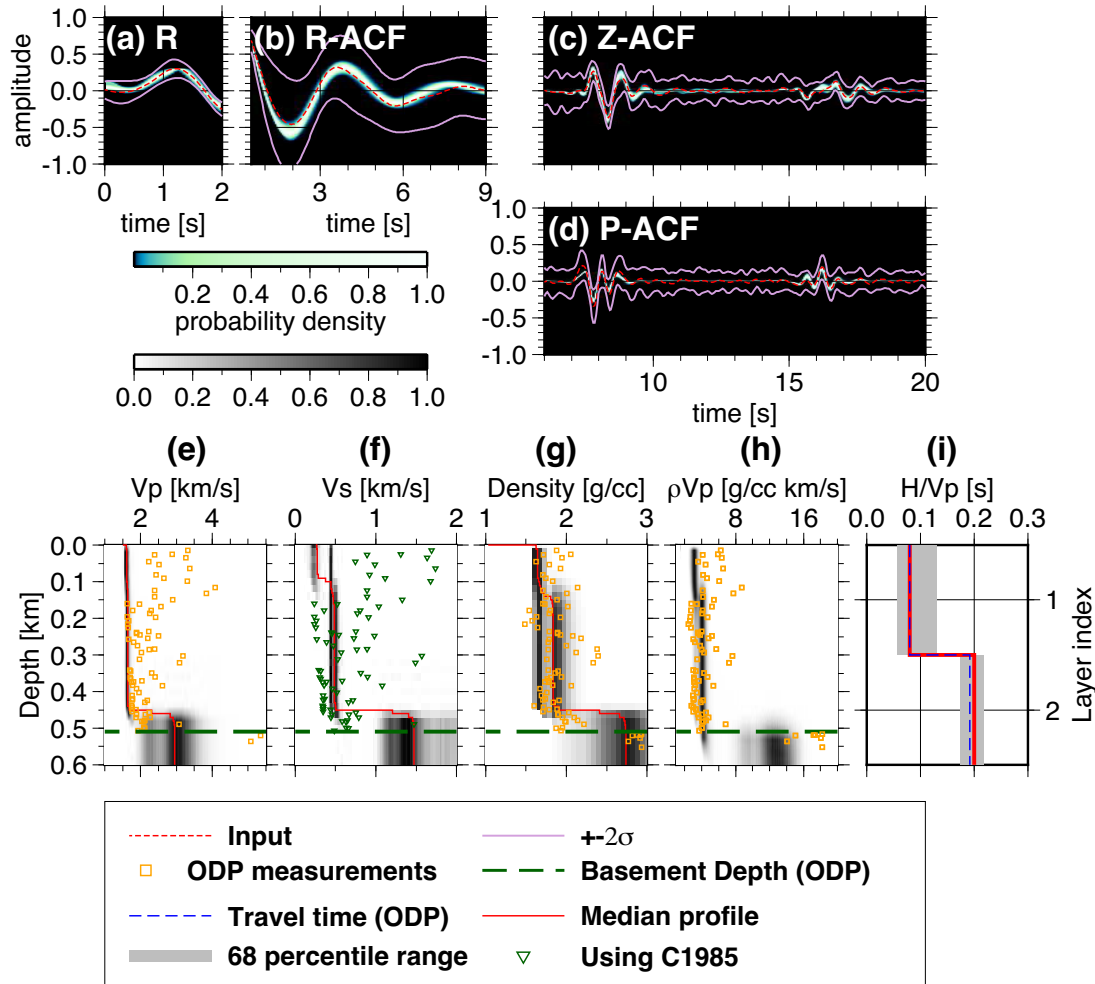
Figure 3. Inversion results for station OL02 of the Oldest-1 array, which is located ∼0.5 km from ODP 802 (Lancelot *et al.* 1990). (a) R-stack, (b) R-ACF, (c) Z-ACF, and (d) P-ACF inversion results, with the probability density distributions of the synthetic waveforms for the searched models in panels (e)–(i) and the input waveforms shown. The background colours present the probability density distribution, with the lighter colors indicating higher probability densities and vice versa. The dashed red lines are the input data waveforms, and the solid purple lines indicate the range of the standard deviation of data noise ($\pm 2\sigma$). The *x*-axis ranges indicate the time ranges used for the inversion. (e)–(h) Probability density distributions of the structures from the inversion and their associated median values (solid red lines). The *y*-axis denotes the depth from the seafloor. (e) *P*-wave velocity (V_P) profile overlain by the direct *P*-wave velocity measurements from the drilling core (yellow squares). (f) *S*-wave velocity (V_S) profile overlain by the *S*-wave velocity converted from *P*-wave velocity using their relationship of mudrocks in Castagna *et al.* (1985) in inverted green triangles (C1985). (g) Density profile overlain by the direct measurements from the core (yellow squares). (h) *P*-wave impedance profile overlain by the product of the *P*-wave velocity and density measurements from the drilling core (yellow squares). The horizontal dashed green lines are the basement depth estimated from ODP drilling. (i) *P*-wave traveltime at layer 1 and layer 2, respectively. The dashed blue lines are the reported traveltimes for ODP Site 802. The solid red lines in panel (i) represent the mode values for each parameter through the sediment layer, with the gray shaded regions denoting the confidence interval (i.e. $\pm\sigma$ around the mode value).

3 METHOD: TELESEISMIC BODY WAVES TO CONSTRAIN SEAFLOOR SEDIMENT STRUCTURE

3.1 Three-component waveforms in use

The reverberation waveform inversion uses the radial, vertical and pressure components of the teleseismic *P*- and/or *S*-wave records from an OBS to effectively extract structural information on low-velocity sediment layers. The stack of the radial component of the teleseismic *P* waves (R-stack) contains the Ps phase converted at the base of the sediment layer. The vertical- and pressure-component autocorrelation functions (Z-ACF and P-ACF, respectively) of the teleseismic *P* waves include *P*-wave reverberations within the water layer and their subsequent coda, which consist mainly of reflections within the sediment layer. The radial component autocorrelation

function (R-ACF) of the teleseismic *S* waves contains the *S*-wave reverberations within the sediment layer.

We use these multicomponent waveforms to estimate the posterior probability of the seismic parameters (V_P, V_S, layer thickness and density) of the 1-D layered structure beneath a station using the Markov chain Monte Carlo approach with parallel tempering (Sambridge 2014). The optimal number of layers is determined by the Akaike Information Criterion (AIC; Akaike 1974). The details of the method are described by Kim *et al.* (2023).

3.2 Selection of frequency ranges and time windows

We filter the Z-ACFs and P-ACFs by applying a 0.5-Hz high-pass filter and Gaussian low-pass filter ($e^{-\omega^2/4a^2}$; $a = 5.0$) to the waveforms. The employed frequency ranges for the R-stacks and R-ACFs are station-dependent (Table S2, Supporting Information).
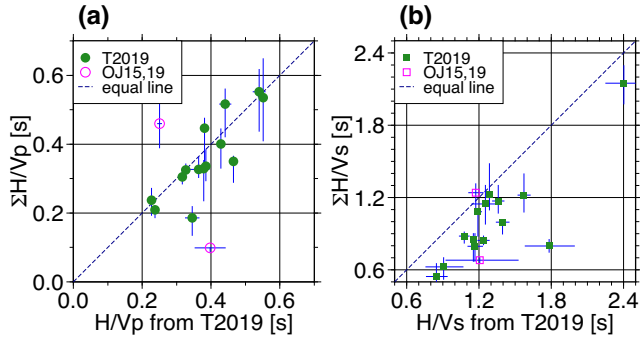
Figure 4. Scatter plots of sediment layer parameters for inversion results of the OJP array (Fig. 1) plotted against the receiver function study T2019 (Tonegawa *et al.* 2019). (a) *P*-wave traveltime (H/V_P) of the sediment, and (b) *S*-wave traveltime (H/V_S) of the sediment at each station in green. Horizontal and vertical blue solid lines in panels (a) and (b) are error ranges from the models of Tonegawa *et al.* (2019) and this study, respectively.

The waveforms for the R-stack are bandpass filtered at 0.5–2.0 Hz for most stations because the high level of microseismic noise in the 0.1–1.0 Hz range hampers the ability to identify signals with high signal-to-noise ratios. However, we use 0.1–1.0 Hz for the Oldest-1 array data due to the low-level noise conditions. The Gaussian low-pass filter parameters for the R-ACFs are chosen using either $a = 1.0$ or 2.5. This choice is determined based on a visual inspection of the peak clarity of the ACFs, noting that a lower frequency range (i.e. smaller a) is preferred for regions with thick sediment and a higher frequency range (i.e. larger a) for regions with thin sediment (e.g. Z6 array). Additional high-pass filters ($f_c = 0.05$ or 0.1 Hz) are applied to the R-ACF in the case of long-period signal exist in the waveform.

The time windows used for the analysis are chosen to include phases related to sediment- and water-layer reverberations. The time windows of the Z-ACF and P-ACF are set to include at least the first two water reverberation phases. The time window of the R-ACF is set to include at least one cycle (one trough and one peak) of the waveform. The zero-lag phase is excluded from the time windows of all ACFs because it has no physical meaning. The time window of the R-stack is set to strictly include the first significant positive amplitude, which is the Ps phase converted at the base of the sediment (i.e. the sediment–crust interface). We use the vertical component without tilt-noise removal because the frequency range of interest (>0.5 Hz) is not affected by tilt noise.

4 RESULTS

4.1 Oldest-1 array

The Z-ACFs in the array exhibit various waveform characteristics (Fig. 2). Most stations possess prominent positive peaks around 7–8 s that represent the first water reverberation. The coda after the first water reverberation phase varies with the station. The variations in the coda of the first water reverberation phase indicate a heterogeneous structure for the sediment layer within the array. Similarly, the P-ACFs show variations in the coda of the water reverberation phase (Fig. S1, Supporting Information). The reverberations in the R-ACFs also vary (Fig. S2, Suppporting Information; $t = 1$–10 s), possibly due to differences in the structures of the sediment layer. The variations in the ACFs are consistent with the
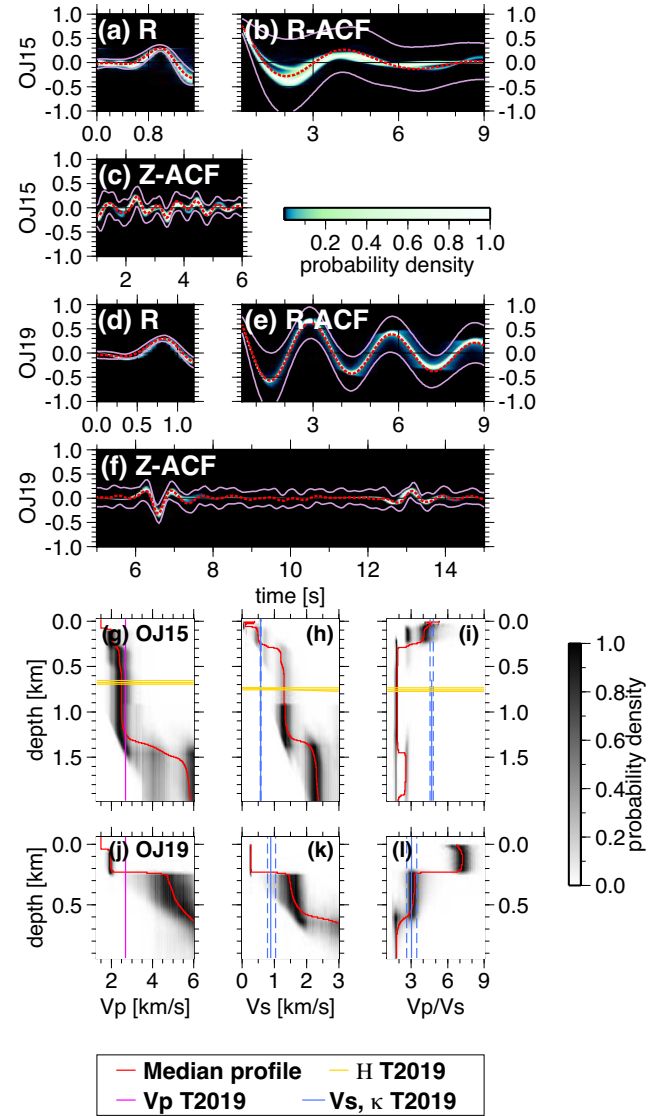

Figure 5. Inversion results for stations OJ15 and OJ19 from the OJP array (see Fig. 1). (a), (d) R-stack, (b), (e) R-ACF, and (c), (f) Z-ACF inversion results, with the probability densities of the synthetic waveforms from the inversion overlain by the observed waveforms at OJ15 and OJ19, respectively. The plotting scheme of (a)–(f) follows that in Figs 3a–c. (g), (j) V_P, (h), (k) V_S and (i), (l) V_P/V_S inversion results, with the probability densities (gray scale) and median values (red solid lines) of the sediment unit shown. The horizontal yellow lines mark the thickness and uncertainty range of the sediment unit from Tonegawa *et al.* (2019). The sediment thickness at station OJ19 is outside of the *y*-axis range in panels (j)–(l). The vertical magenta lines in panels (g) and (h) represent $V_P = 2.7$ km s^{-1}, which is the assumed velocity in Tonegawa *et al.* (2019). The solid and dashed blue lines in panels (h), (k) and (i), (l) denote the V_S and V_P/V_S profiles, and their uncertainty ranges from Tonegawa *et al.* (2019), respectively.

complex bathymetry (i.e. the presence of seamounts) within the array, thereby implying a variable sediment thickness across the array. Station OL09 does not possess a clear first water reverberation peak, which is expected at 7–8 s due to the station depth (Fig. 2; Fig. S3, Supprting Information). We therefore considered this station has an atypical vertical component record and exclude the Z-ACF for station OL09.

We compare the results at station OL02 with the nearby active-source seismic analysis and drilling core sample measurements at
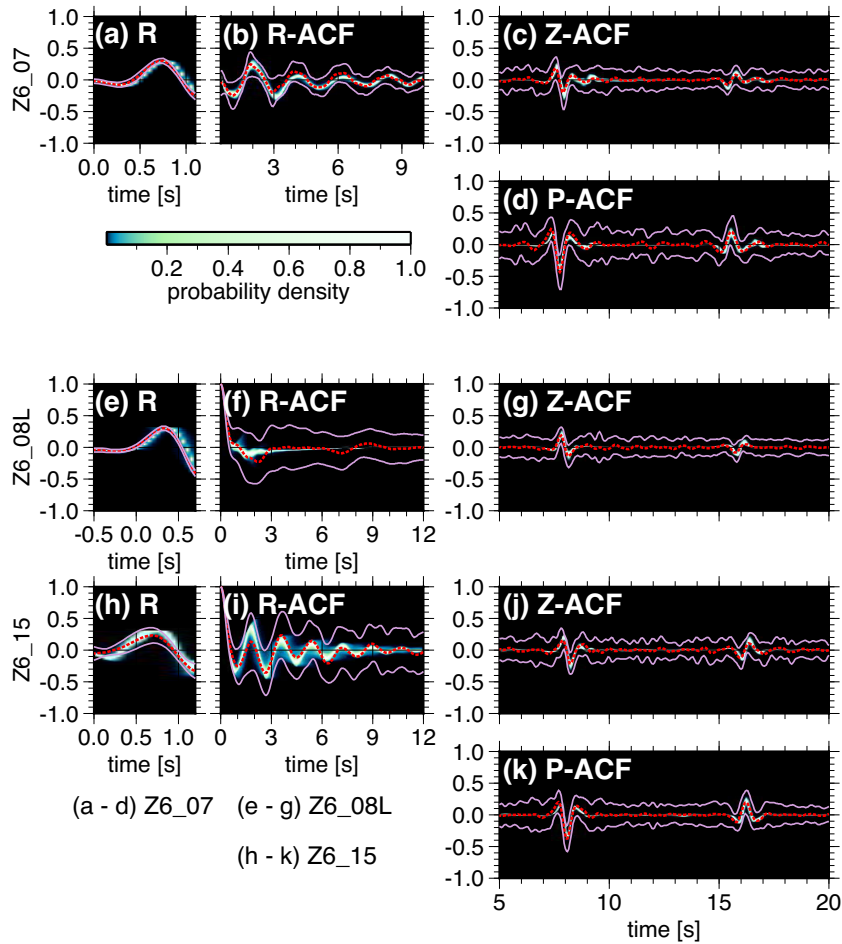
Figure 6. Inversion results for three stations from the Z6 array in the Northwest Pacific (see Fig. 1). (a) R-stack, (b) R-ACF, (c) Z-ACF and (d) P-ACF inversion results, with the probability densities of the synthetic waveforms from the inversion overlain by the observed waveforms at station Z6_07. Also shown are probability density distributions of synthetic waveforms overlain by the observed waveforms at stations (e)–(g) Z6_08L and (h)–(k) Z6_15, respectively. The presentation of the inversions results follows that in Figs 3(a)–(d).

ODP leg 129 site 802 (Lancelot *et al.* 1990). The ODP site provides V_P (Fig. 3e) and density (Fig. 3g) measurements from drilling core samples, and the active-source seismic survey provides the traveltimes between seismic reflectors (Fig. 3i). The structure can be parameterized into four solid layers at station OL02 to produce waveforms that explain the R-stack (Fig. 3a), R-ACF (Fig. 3b), Z-ACF (Fig. 3c), and P-ACF (Fig. 3d).

The upper two layers of this four-layer model are sediment layers with $V_P < 4.1\,\mathrm{km\,s^{-1}}$ and $V_S < 2.0\,\mathrm{km\,s^{-1}}$ (Figs 3e and f). As discussed by Kim *et al.* (2023), the *P*-wave impedance (Fig. 3h) and traveltime for each layer (Fig. 3i) agree well with the ODP site estimates compared with either the individual V_P or density measurements (Figs 3e and g, respectively). The V_P values from the samples have a large degree of scatter, whereas the model from the inversion is sharply confined (Fig. 3e). The basement crust impedance (Fig. 3h) and total sediment thickness (Figs 3e–i) are also consistent between our inversion estimates and the direct drilling measurements. The active-source seismic survey at the ODP site does not provide V_S estimates, whereas the results from reverberation waveform inversion can provide the V_S structure (Fig. 3f) by using the radial-component waveforms (Figs 3a and b). The V_S values converted from V_P using their relationship in mudrocks (Castagna

et al. 1985) greatly differ from the inverted V_S structure. This difference is likely due to the difference in sediment composition, that the sediments have volcanic origin near OL02.

4.2 Ontong Java Plateau array

Tonegawa *et al.* (2019) conducted receiver function analyses to model the sediment layer assuming a single sediment layer. We compare their results with those of this study in terms of the summations of H/V_P (i.e. *P*-wave traveltime, where H is the sediment layer thickness) and H/V_S (i.e. *S*-wave traveltime) of the sediment layer (Fig. 4). The general positive correlations of the estimated parameters indicate the overall agreement between the two approaches. The intrasediment discontinuities that have been resolved via our method will lead to improved predictions of sediment amplification and the reverberation effect (Kim *et al.* 2023).

Stations OJ15 and OJ19 differ in the total sediment thickness significantly (Fig. 5). Total sediment thicknesses of 1.079 and 0.195 km are obtained at stations OJ15 and OJ19, via our method, which are thicker (Fig. 5g) and thinner (Fig. 5j) than the associated receiver function estimates (0.676 and 1.093 km; Tonegawa *et al.* 2019), respectively. The Z-ACF for station OJ15 is complicated due to
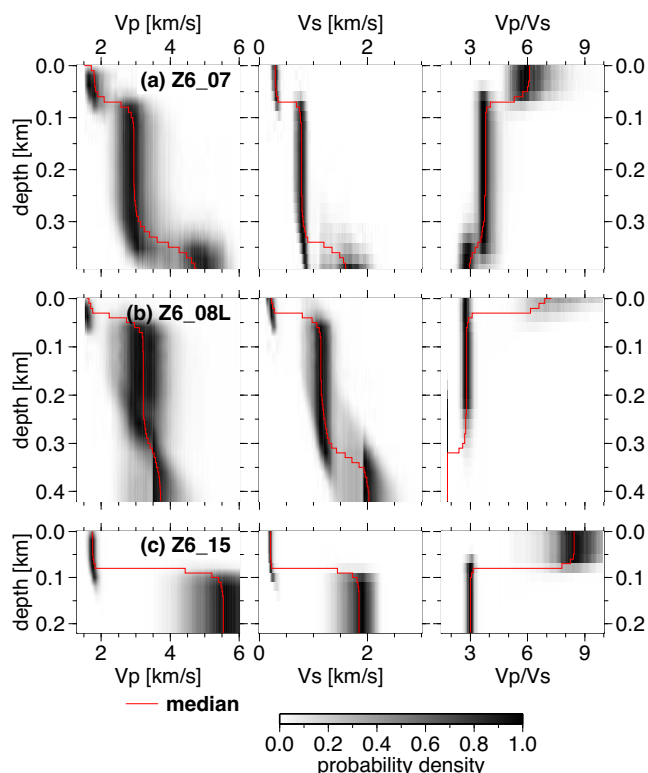
Figure 7. Inversion results for three stations from the Z6 array using the input waveforms in Fig. 6. (Left) V_P, (middle) V_S and (right) V_P/V_S inversion results for stations (**a**) Z6_07, (**b**) Z6_08L, and (**c**) Z6_15. The presentation of the inversion results follows that in Figs 3(e)–(g).

4.3 Z6 array

The teleseismic body-wave waveforms of the stations in the Z6 array show characteristics that are indicative of thin sediment layers (Fig. 6). The R-stack waveforms (Figs 6a, e and h) have delays of <1 s relative to the R-stack peak, which are shorter than the delays observed at stations OL02 and OJ15 (Figs 3a and 5a, respectively). The time intervals between peaks and troughs in the R-ACFs are shorter and their amplitudes are smaller (Figs 6b, f and i) than those observed at the stations in the Oldest-1 array (Fig. S2, Supporting Information). The times between the first water layer reverberation (positive peak) and the following sediment layer reverberation (negative peak) in the Z-ACFs and P-ACFs are also shorter than those observed in the Oldest-1 array (Fig. 2 and Fig. S1, Supporting Information). These observations imply that the sediment beneath these stations is thinner than that beneath the Oldest-1 array.

The sediment thicknesses are <350 m throughout the array (Fig. 7). The largest velocity contrast for station Z6_08L is located at 44.65 m (Fig. 7b), which explains the absence of peaks and troughs in the R-ACF (Fig. 6f). The global sediment model (Laske *et al.* 2013) indicates a 19.9–59.5 m thickness of sediment in the region, which is consistent with the depth of the sharpest discontinuity. Our definition of sediments ($V_P < 4.1$ km s^{-1} and $V_S < 2.0$ km s^{-1}) yields a thickness of ∼300 m for station Z6_08L (Fig. 7b). The large V_P range of 3.0–5.5 km s^{-1} for the crustal basement (Fig. 7) is consistent with the broad V_P range (2.5–5.2 km s^{-1}) reported at nearby ODP site 878 (Premoli Silva *et al.* 1993). All stations commonly show increasing V_P and V_S with depth, while the V_P/V_S values decrease with depth. Furthermore, the sediment layer is thicker beneath station Z6_07 (Fig. 7a) than beneath the other stations of the Z6 array (Figs 7b and c), and is divided into a thin upper layer with high V_P/V_S and a thick lower layer with low V_P/V_S (boundary at ∼0.1 km).

4.4 7D and YS arrays

Fig. 8 shows the waveforms for selected stations from the 7D (J11D in Figs 8a–d; J28D in Figs 8e–g) and YS (PL37 in Figs 8h–k; PL46 in Figs 8l–o) arrays. The results indicate a two-layered sediment structure in the region of thick sediment within the 7D array and a one-layered sediment structure within the YS array (Fig. 9). At station PL37, the impedance from the drilling sample measurements (Fig. 9g) and total sediment thickness (Figs 9e–g) from ODP site 843 are in close agreement with the values derived from the reverberation waveform inversion.

The V_S profile from the Rayleigh-wave admittance measurements (Bell *et al.* 2015) is similar to the layered structure from our analysis (Figs 9b and d). The two V_S models overlap at the shallowest depth (<0.05 km; Figs 9b and d) and deviate below a sharp Vs contrast at ∼0.05 km at J11D (Fig. 9b) and ∼0.10 km at J28D (Fig. 9d). The total sediment thicknesses estimated from Rayleigh-wave admittance (Figs 9a–d; Bell *et al.* 2015) and seafloor compliance (Figs 9e–i; Doran & Laske 2019) are always thinner than the estimates from the reverberation waveform inversion. However, the sediment thicknesses estimated from the seafloor drilling measurements (Figs 9e–i) are consistent with our estimations at stations PL37 (Fig. 9f) and PL46 (Fig. 9i). Note that the sediment thickness estimated at station PL46 from drilling measurements is a minimum estimate; consequently, our estimates are preferred to those of Doran & Laske (2019).

The discrepancies in sediment thickness between our method and previous studies may be explained by the trade-offs between the effects of sediment thickness, velocity (V_P and V_S) and density on

the short-time interval between the shallow water reverberations (Fig. 5c). The positive and negative phases at ∼2.4 and ∼4.8 s are the first and second water-layer reverberations, respectively, with the negative phase at ∼3.5 s indicating a thick sediment layer with a two-way *P*-wave traveltime of >1 s. However, the sediment model of Tonegawa *et al.* (2019) does not explain the phase at 3.5 s. The thickness of the sediment layer at station OJ19 is 1.093 km, as deduced from a receiver function study (Tonegawa *et al.* 2019), which is much thicker than the estimate from our reverberation waveform inversion (0.195 km). The timing of the peak in the R-stack for OJ19 (Fig. 5d) is shorter than its timing for OJ15 (Fig. 5a), which indicates the presence of a thinner sediment layer at OJ19 than at OJ15, thereby supporting our thinner sediment model.

The two-way traveltime within the water layer is short for stations in shallow water, such that the multiple orders of water- and sediment-layer reverberations constructively and/or destructively interfere with each other in the receiver functions and autocorrelation functions. Furthermore, if the structure is complex (e.g. the presence of a thin sediment layer), then the choice of the filter range may inhibit the ability to distinguish the timing of the peaks of the reverberation phases, which is a key for *H*-*κ* stacking with receiver functions. The reverberation waveform inversion has strength in using waveforms for structural inversion, which can reduce such an ambiguity in the phase identification. Another strength of our method comes from the ability to utilize multicomponent waveforms that give information on both the *P*- and *S*-wave reverberations separately. The strengths of our method are enhanced for shallow-water OBSs and the presence of thin sediment layers where the higher-order multiples of *P*- and *S*-waves overlap closely in time.
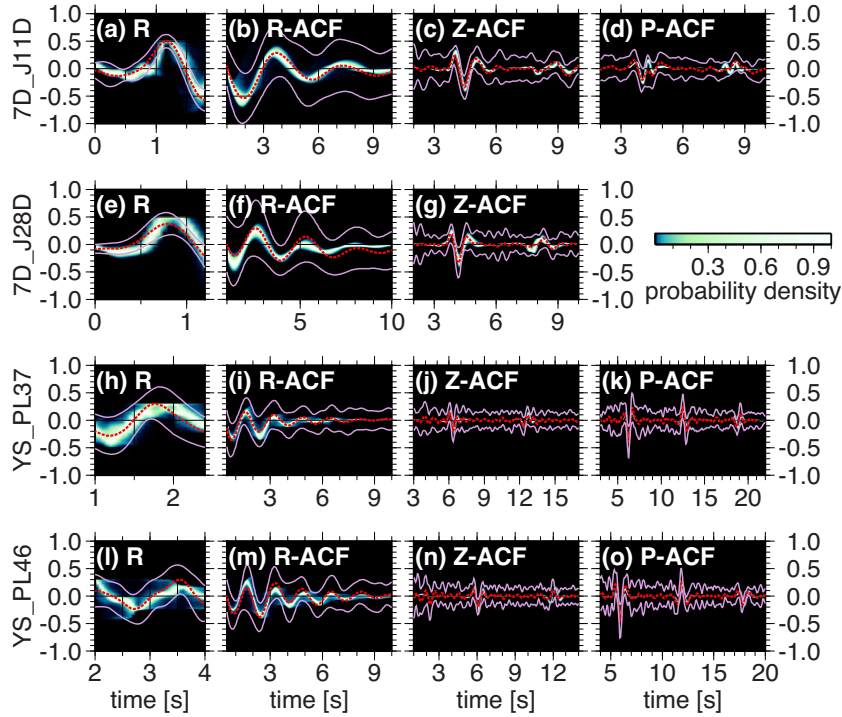
Figure 8. Inversion results for stations from the YS and 7D arrays (Fig. 1). The synthetic seismograms used for the probability density function are from the models in Fig 9. (a)**,** (e)**,** (h)**,** (l) R-stack, (b), (f), (i), (m) R-ACF, (c), (g), (j), (n) Z-ACF and (d)**,** (k)**,** (o) P-ACF inversion results for stations J11D and J28D in the 7D array, and stations PL37 and PL47 in the YS array. The presentation of the inversion results follows that in Figs 3(a)–(d).

Rayleigh-wave admittance and seafloor compliance analyses. Fig. S4 (Supporting Information) shows that the predicted body-wave waveforms generated using sediment models from the Rayleigh-wave admittance method (Bell et al. 2015) and reverberation waveform inversion are different. Therefore, the non-uniqueness of the Rayleigh-wave admittance may result in the different sediment models in Figs 9(a)–(d). Rayleigh-wave admittance is discussed further in Section 5.

The probability density function of V_S in station PL37 has two high-probability regions at depths >0.25 km (Fig. 9f). Similarly, multiple high-probability density regions are observed in Figs 5(g)–(f) for station OJ15. For the final preferred model, we choose the modes of parameters since often we can distinguish a peak with the larger probability within the multimaxima. If the probabilities of multimaxima are comparable (e.g. Fig. 9f), other data sets that can distinguish the two models would be required to resolve the parameter.

4.5 Short-period seismic sensor: S6N09

We use the five-year records (2017 April to 2022 May) from station S6N09 to construct the waveform data (R-stack, R-ACF and Z-ACF; Figs 10a–c, respectively). The large number of events that are used to generate the R-stack yielded a bootstrap stacking error of the R-stack that is too small to use for inversion, resulting in an overfit to the R-stack waveform and a poor fit to the other autocorrelation waveforms. To maintain balance between the different data sets, the standard deviations (i.e. σ) were used for weighting the likelihood of the P-, R-, and Z-ACFs, and the standard error (i.e. $\sigma/\sqrt{n}$, where n is the number of waveforms before stacking) is used for the R-stack in the reverberation waveform inversion. Given the small error for the R-stack, we alternatively use the bootstrap error of the

stacked autocorrelation functions for station S6N09, as opposed to the standard deviation used for other stations (Sections 4.1–4.4), to avoid overfitting the R-stack.

The inverted velocity model indicates a sediment layer of ~0.5 km thickness at station S6N09 (Figs 10d and e). We compare the sediment thickness, V_P, and V_P/V_S from other studies that employed active-source seismic surveys (Fujie *et al.* 2013; Nakamura *et al.* 2014). The well-resolved top layer V_P and V_P/V_S for the upper 100 m of the sediment layer ($V_P/V_S \sim 8$) agree with V_P and V_P/V_S values from Fujie *et al.* (2013) (Figs 10d and e). Furthermore, the inverted V_P/V_S decreases with depth and agrees with the average V_P/V_S value from the active-source study by Nakamura *et al.* (2014). We test the inversions with shorter time spans that are similar to typical broad-band OBS deployment and short-period OBS deployment (3 months to 1 year). Smaller numbers of events are stacked to make input waveforms (Table S3, Supporting Information) which results in slightly larger data noise that do not impact on the final models. The results of inversions are consistent with the 5-year-long data (Fig. S7, Supporting Information). These consistencies indicate that the reverberation waveform inversion has a resolution that is comparable to that of active-source seismic surveys.

5 DISCUSSION

Our results from OBS stations in various water depths and sediment structural settings show that the sediment models from the waveform inversion are in good agreement with seafloor drilling measurements (Fig. 3) and seismic models from active-source seismic analyses (Fig. 10). The consistent sediment layer thicknesses, and P-wave impedance, P-wave traveltime and V_P/V_S profiles through the sediment layer at the stations presented in Figs 3, 9, and 10
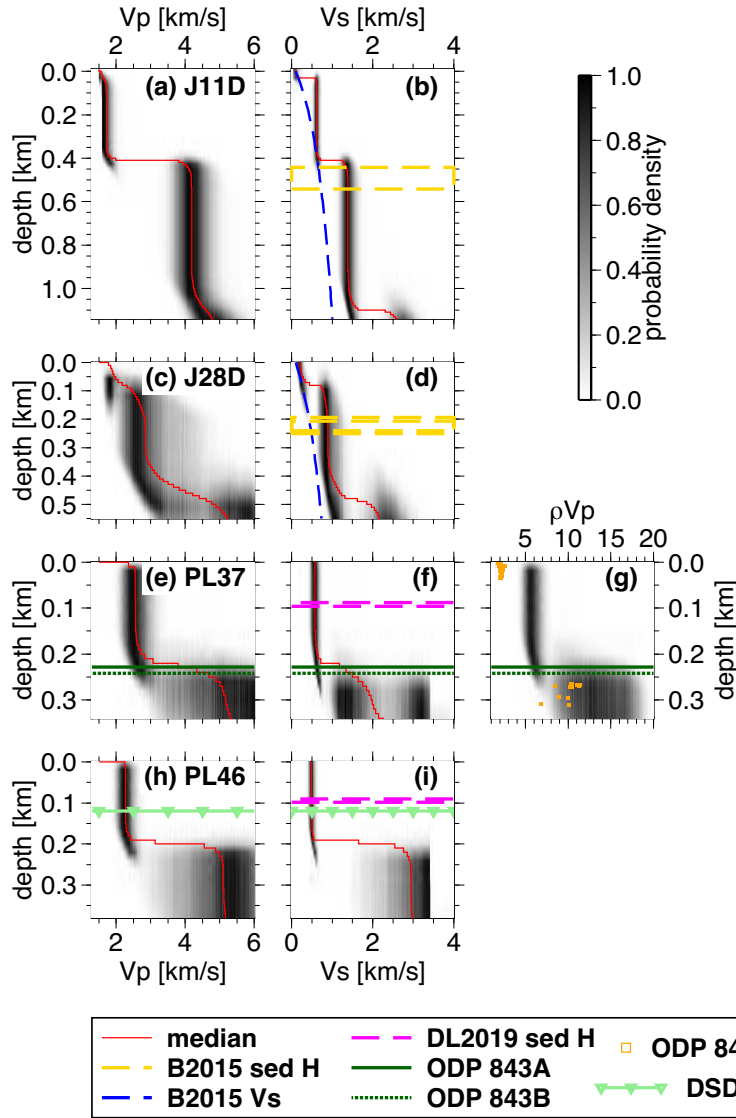
Figure 9. Inversion results for the stations in Fig. 8. (a), (c), (e), (h) V_P, (b), (d), (f), (i) V_S and (g) P-wave impedance inversion results, with the probability densities and median values (red lines) of the sediment unit shown. The dashed blue curves and dashed horizontal yellow boxes in panels (b) and (e) are the array V_S profile and depth range of the sediment basement from Bell *et al.* (2015), respectively. The yellow small squares in panel (g) are the product of the P-wave velocity and density measurements from the drilling cores at ODP Sites 843A–C. The solid and dotted horizontal dark-green lines in panels (e)–(g) mark the depth of the sediment unit at ODP Sites 843A and 843B near station PL37, respectively. The light-green line with inverted triangles in panels (h) and (i) marks the minimum thickness of the sediment unit that is indicated from DSDP Site 67. The dashed horizontal magenta boxes in panels (f) and (i) mark the range of depth range of the sediment basement, from Doran & Laske (2019).

validate the broad applicability of our method to a wide range of OBSs installed on the seafloor.

5.1 Laterally heterogeneous sediment structures in the Pacific

As anticipated from the large variations in Z-ACFs among the stations in the Oldest-1 array (Fig. 2), the total sediment thickness from the waveform inversion (Fig. S5, Supporting Information) varies from a few hundred meters to 1000 m. There are also non-uniform V_P and V_S profiles through the sediment layer. For example, stations OL02, OL04, and OL07 show either a decrease or minimal increase in V_P from the upper to lower layer (Fig. S5, Supporting Information), whereas other stations show a sharp increase in V_P

where a sharp increase in V_s is present. There is an enigmatic velocity drop at ∼0.6 km depth in station OL10 from the waveforms, the reliability should be investigated with different approaches. This lateral heterogeneity within the array is also observed within other arrays in this study, such as the stations within the Z6 array showing either one- or two-layer sediment structures.

These lateral heterogeneities in sedimentary structure contain much shorter-wavelength components than those observed in the global model (e.g. CRUST1.0; Laske *et al.* 2013; Straume *et al.* 2019). The number of sublayers is not constant, which is different from the mostly single-layer sediment layer in CRUST1.0. The decrease in V_P/V_S from >9 to <2 toward the basement (Fig. 11d) implies that V_S varies significantly throughout the sediment unit. Our analysis of the shallow layers via reverberation waveform inversion
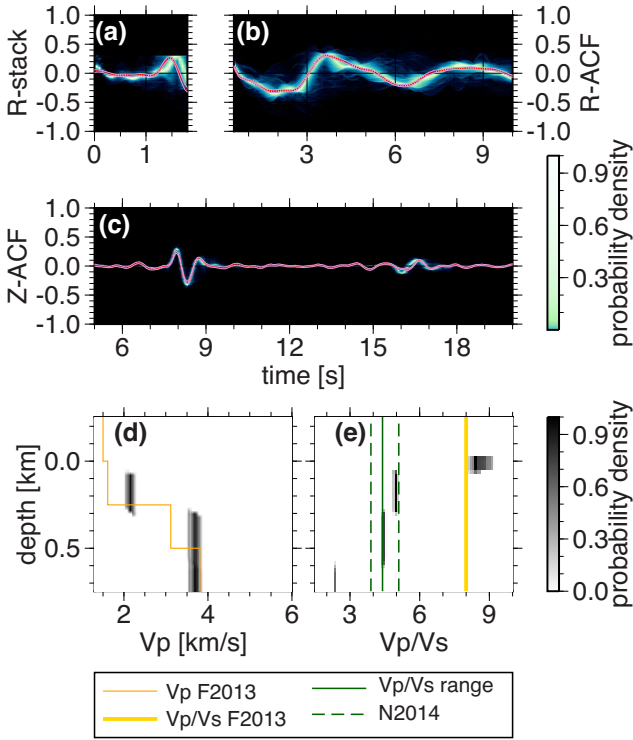
Figure 10. Inversion results for station S6N09, which is located at the outer-rise region of the Northeast Japan subduction zone. (a) R-stack, (b) R-ACF and (c) Z-ACF inversion results, with the probability density distributions of the synthetic waveforms for the searched models in panels (d) and (e) overlain by the input waveforms with noise. The presentation of the inversion results follows that in Figs 3(a)–(c). (d) *P*-wave velocity probability density function from the inversion, overlain by V_P model from the active-source seismic survey of Fujie *et al.* (2013). The orange profile shows the V_P profile from the active-source seismic survey at the nearest point to station S6N09 in Fujie *et al.* (2013). (e) V_P/V_S probability density function by depth, overlain by the estimates from the active-source seismic surveys in the area (Fujie *et al.* 2013; Nakamura *et al.* 2014). The solid and dashed green lines mark the V_P/V_S and its uncertainty range above the top of basement crust, from Nakamura *et al.* (2014). The thick yellow line marks the average V_P/V_S ratio of the sediment layer above a conversion interface, from Fujie *et al.* (2013).

enables a discussion of the presence and degree of heterogeneity in the shallow sedimentary structure.

5.2 Implications of the sediment structure

The sediment models in this study show that even the sediment layers with a thickness of <500 m possess 1–2 intrasediment discontinuities (e.g. station S6N09 in Fig. 10). For a given top layer V_S and fixed other parameters for the crust layer and the half-space (e.g. below the Moho), the amplitude of the *P*-to-*S* converted phase at the Moho passing through the sediment sublayers increases as the number of discontinuities increases (Fig. 11a), with an inferred upper limit of amplification (Fig. 11a). Knowledge of the presence of sediment discontinuities will therefore allow us to better predict the amplification of body waves that are observed as systematic large amplitudes in receiver functions from OBSs (e.g. Kim *et al.* 2021; Dai *et al.* 2023). Our use of the AIC to determine the optimal number of parameters is particularly important in enabling us to identify the lower limit of amplification via the sediment layers,

given the preference of the AIC for smaller unknowns (i.e. number of layers).

We plotted V_P/V_S versus V_P (Fig. 11c) and the probability density function of V_P/V_S as a function of sediment depth (Fig. 11d) for the sediment models from all the analyzed OBSs. Fig. 11(c) shows that the V_P/V_S values in the top sediment layer are higher than those from previously known relationships (e.g. Hamilton 1979; Castagna *et al.* 1985; Brocher 2005) compiled from laboratory-based measurements. Especially, the discrepancy is evident when $V_P < 1.8$ km s^{-1} where the V_P/V_S gets higher. The higher V_P/V_S values of the top layer from our study compared with the laboratory-based measurements are plausible considering that these *in situ* uppermost sediments are more water-saturated than the samples analyzed in the laboratory. If we consider the *in situ* sediment velocity can be approximated by a mixture of dry sediment and water, $V_P = V_{P_0}(1 - x) + V_{water}x$ and $V_S = (1 - x)V_{S_0}$, where V_{P_0} and V_{S_0} are the *P*-wave velocity and the *S*-wave velocity of the dry sediment, respectively, x quantifies the contribution of water ranging from 0 to 1, and V_{water} is the *P*-wave velocity of water. Then, we can obtain the following relationship between V_P and V_P/V_S as

$$\frac{V_P}{V_S} = \frac{V_{P_0}}{V_{S_0}} + \frac{V_{water}}{V_{S_0}} \cdot \frac{V_{P_0} - V_P}{V_P - V_{water}}, \tag{1}$$

which indicates that V_P/V_S becomes large as V_P gets close to V_{water} as seen in the data. Our preferred model, assuming $V_{water} = 1.5$ (**km s^{-1}**), that fits our inverted (V_P, V_P/V_S) of the top sediment layer (Fig. 11c, red triangles) and does not go far below other empirical relationships is given by $V_{P_0} = 2.55$ km s^{-1} and $V_{S_0} = 1.66$ km s^{-1}. Then, the V_P/V_S ratio is,

$$\frac{V_P}{V_S} = 0.633 + \frac{0.949}{V_P - 1.5}, \tag{2}$$

which is the thick light gray curve in Fig. 11c. However, we still observe significant variations from this regression curve, with the lower bound being approximately defined by the regression curve from Hamilton (1979) (solid light-blue curve in Fig. 11c). The equation that defines the upper bound of V_P/V_S may be given by

$$\frac{V_P}{V_S} = 1.61 + \frac{2.42}{V_P - 1.5} \tag{3}$$

that is shown by the thin gray line in Fig. 11(c). Furthermore, V_P/V_S is greater than ~6 for a sediment layer that is shallower than ~100 m (Fig. 11d).

V_P/V_S values are critical in predicting the strength of the shallow-layer reverberations affecting OBS body-wave records (Kim *et al.* 2023). The higher V_P/V_S values in Figs 11(c) and (d) indicate stronger seafloor sediment reverberations than the cases that have been predicted using known relationships (Hamilton, 1979; Brocher 2005).

Both *P*- and *S*-wave reverberations affect the radial component of teleseismic *P*-waves and their associated coda in OBS records, whereas land station records are only affected by *S*-wave reverberations (Yu *et al.* 2015). Fig. 11(b) shows that the PP^{up}PP^{down} signal increases as V_P decreases in the top layer (i.e. V_P/V_S increases), which implies that the reverberation phases recorded by the radial component include more PwPps phases (Fig. S8, Supporting Information). Furthermore, the PP^{up}PS^{down} signal is small, which implies negligible PwPss phases. The coda waves from the multi-layered structure with a high V_P/V_S in the top layer will deviate from the monotonic *S*-wave oscillation due to a mixture of PwPps
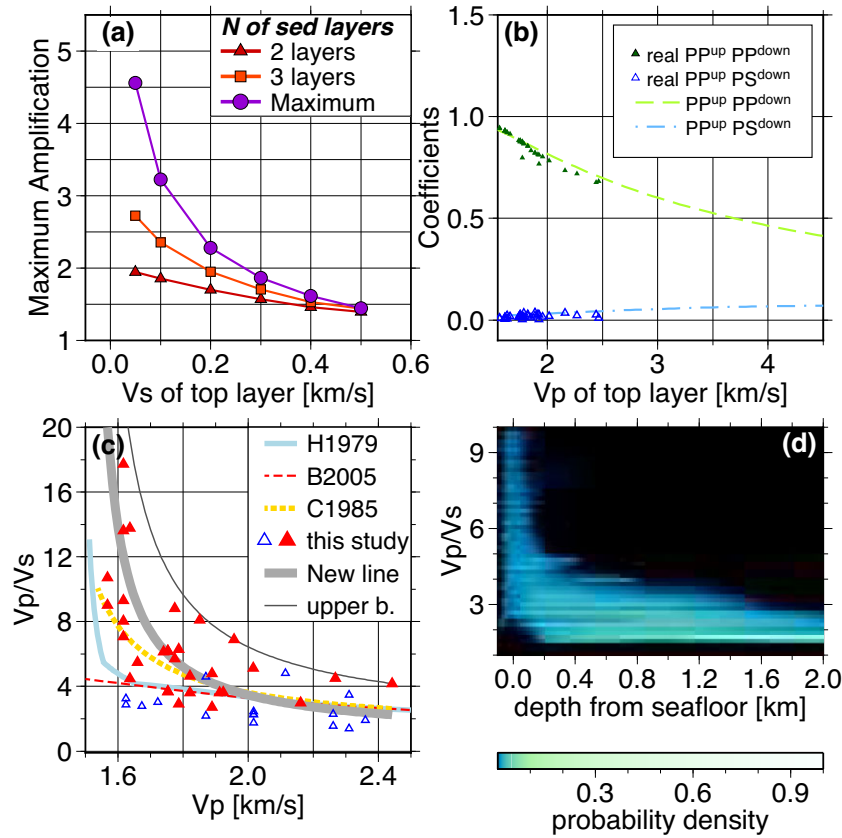
Figure 11. (a) Maximum possible amplification of the *P*-to-*S* converted phase at the base of the sediment layers under various circumstances. The basement $V_S = 1.0 \, \mathrm{km \, s^{-1}}$ and V_S of the top layer varies along the *x*-axis (Table S4, Supporting Information). The red triangles, orange squares, and purple circles denote the cases of two sediment layers (a single intrasediment discontinuity), three sediment layers (two intrasediment discontinuities) and infinite sediment layers, respectively. (b) Products of the *P*-to-acoustic phase (PP^{up}) and acoustic-to-*P* phase (PP^{down}) or acoustic-to-*S* phase (PS^{down}) across the water–sediment boundary (Fig. S8, Supporting Information), with different sediment velocities assumed (Table S5, Supporting Information). The triangles are the product of the computed transmission coefficients using the sediment velocity models from the stations in Fig. 1. (c) V_P/V_S versus V_P from the stations in Fig. 1. The filled red triangles and open blue triangles are the (V_P, V_P/V_S) pairs from the top sediment layer and the remaining sediment layers. The thick gray curve is eq. (3) that fits the red triangles. The thin gray curve is the fit of upper boundary values expressed as eq. (4). The solid light-blue, thin dashed red, and thick dashed yellow curves are the V_P/V_S versus V_P plots using the empirical relationships of Hamilton (1979), Brocher (2005) and Castagna *et al.* (1985), respectively. (d) Probability density function of V_P/V_S by depth below the seafloor using the results from the stations in Fig. 1.
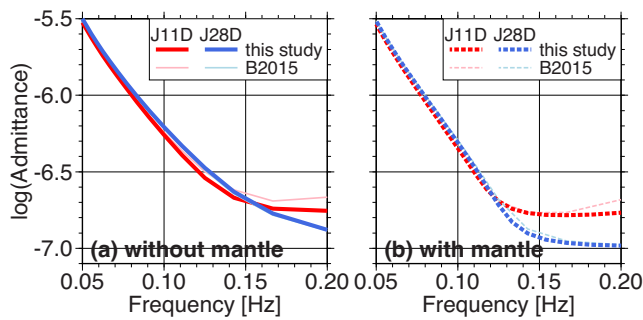

Figure 12. Predicted Rayleigh-wave admittance using the sediment models at stations J11D (red) and J28D (blue) within the 7D array. The thick lines are predictions using the sediment models from this study. The thin lines are predictions using the models of Bell *et al.* (2015) ('B2015'). The predictions were made using a half-space model comprising (a) water, sediment, and crust, and (b) water, sediment, crust, and mantle. The crust and mantle layers assumed by Ruan *et al.* (2014) and Bell *et al.* (2015) (Table S6, Supporting Information) are added to our model to compute our predictions in panel (b).

phases after the water *reverberation*. This implies that the reverberations recorded in the radial component will contain a mixture of *P*- and *S*-wave reverberations (e.g. PwPps phases), thereby deviating from the pure *S*-wave reverberations in the sediment layer of terrestrial sedimentary basins (Yu *et al.* 2015). Therefore, this additional complexity should be considered when constructing filters to remove the reverberations due to shallow sediment layers in ocean environments.

5.3 Comparison with Rayleigh-wave admittance methods

Fig. 12 compares the calculated Rayleigh-wave admittance for the sediment models from our waveform inversion with those for models from a Rayleigh-wave admittance analysis (7D_J11D and 7D_J28D; Bell *et al.* 2015). Our models do not include the crust and uppermost mantle layers, whereas the Rayleigh-wave admittance analysis of Bell *et al.* (2015) assumes a crust and mantle model from an independent study to invert for the sediment layer. The predicted Rayleigh-wave admittance from our model and that of Bell *et al.* (2015) show overall agreement after either removing the crust and mantle layers from the Bell *et al.* (2015) model (Fig. 12a) or

adding the same crust and mantle layers to our model (Fig. 12b). This indicates that our sediment model is generally consistent with the Rayleigh-wave admittance observations, but with finer structural details that explain the reverberation waveforms.

While there is a general agreement between Rayleigh-wave admittance, the radial-to-vertical component ratio of the Rayleigh wave (i.e. ellipticity) differs between the two models (Fig. S9, Supporting Information), thereby indicating the possibility of obtaining additional structural constraints from our waveform inversion. The Rayleigh-wave admittance has often been used for sediment inversion when good crustal models are available (Ruan *et al.* 2014; Bell *et al.* 2015; Saikia *et al.* 2020). We instead suggest using the presented sediment reverberation inversion method to first determine the fine sediment structure. The Rayleigh-wave admittance or ellipticity can then be used to constrain the structure at greater depths. Alternatively, the overall crustal structure can be obtained simultaneously through jointly inverting all together. Combining the measurements from Rayleigh wave amplitudes may enable us to resolve existing velocity gradients that occur by compaction which was not possible with the current body wave-based method.

5.4 Applicability of the method to general OBSs

Kim *et al.* (2023) tested the reverberation waveform inversion method using only a BBOBS from Japan (Suetsugu & Shiobara 2014). The noise properties of an OBS are dependent on the instrument design and seismic sensor (Janiszewski *et al.* 2023). The noise spectra of broad-band OBSs from Japan and US (fig. 2 in Suetsugu & Shiobara 2014; fig. 2 in Janiszewski *et al.* 2023) differ in the <1 Hz frequency range, which may impact the amplitudes in the ACFs used in the present analysis. Therefore, a difference in the compatibility of the waveform inversion to the US BBOBSs is expected. However, we have demonstrated that the presented body-wave reverberation waveform inversion method yields sediment models that are in good agreement with seafloor drilling observations, regardless of the specifications of the selected OBSs (Table S1, Supporting Information). The results indicate that the presented method can be applied to a wide range of OBSs with different noise spectra.

Various approaches have been developed to image the seafloor sediment structure via OBS data inversion, and numerous studies have used long-period signals that target either fundamental mode Rayleigh-wave admittance or seafloor compliance (e.g. Ruan *et al.* 2014; Bell *et al.* 2015; Saikia *et al.* 2020; Mosher *et al.* 2021). However, a smooth profile is generally assumed due to the insensitivity of these approaches to sharp velocity jumps in the long-period measurements. The body-wave reverberation waveform inversion method presented in this study can image sediment structures at a resolution that is comparable to those obtained from active-source seismic measurements, thereby providing critical constraints for body-wave-based methods for studies of the deeper Earth, such as receiver function, shear-wave splitting and seismic tomography studies, that utilize OBS data.

6 CONCLUSIONS & SUMMARY

We have used the teleseismic body-wave records from OBSs deployed in the Pacific Ocean to characterize the properties of shallow sediment. The reverberation waveform inversion method demonstrated a high degree of agreement with sediment models inferred from nearby drilling sample measurements and local active-source

seismic surveys, regardless of the location and OBS type. The types of OBSs used in this analysis include BBOBSs from Japan (Figs 3 and 5) and the US (Figs 7 and 9) and a short-period strong-motion sensor (S-net; Fig. 10).

This wide applicability of the method allows for the degree of heterogeneity in the shallowest structure to be evaluated in future OBS array deployments. Consequently, the results will be useful for array-wise analyses (e.g. stacking throughout the array) to avoid the influence of heterogeneous shallow layers.

The estimated V_P/V_S values for the seafloor sediment models are higher than those expected from previous studies. We believe the proposed method will yield improved predictions of the impact of the water and sediment layers in body-wave records and the amplitude and phase of the surface-wave or seafloor compliance records from OBS observations.

SUPPORTING INFORMATION

Supplementary data are available at *GJIRAS* online.
    Kim_et_al_GJI_SOM_new.pdf

Figure S1. The stacked P-ACFs calculated using teleseismic P-waves (blue) at each station of the Oldest-1 array. The autocorrelation functions are calculated with the same parameters as Figure 2. The notations are the same as Figure 2 in the main text.

Figure S2. The stacked R-ACFs calculated using teleseismic S-waves (blue) at each station of the Oldest-1 array. Radial autocorrelation functions are calculated with the Gaussian low-pass parameter a = 1.0 and the whitening window width W = 0.5. The notations are the same as Figure 2 in the main text.

Figure S3. Autocorrelation functions of pressure (red) and vertical (green) components at station OL09. The first water reverberation at 7–8 sec is not clear on the vertical component, while it is evident on the pressure component.

Figure S4. Synthetic waveforms at station J11D of the 7D array using sediment velocity models from Bell *et al.* (2015) and this study ("this study") overlapped with the observed waveforms. Waveforms of (a) radial stack (R-stack), (b) radial autocorrelation function (R-ACF), (c) vertical autocorrelation function (Z-ACF), and (d)

pressure autocorrelation function (P-ACF). (a,c–d) are calculated using incident P-wave with a ray parameter of 6.5 ´ 10−5 s/m. (b) is calculated with incident S-wave with a ray parameter of 1.2 ´ 10−4 s/m. (a) is band-pass filtered with 0.1–1.0 Hz, (b) is low-pass filtered with Gaussian lowpass filter parameter a = 2.5 and calculated with smoothing width W = 0.5, and (c,d) are 4 low-pass filtered with Gaussian low-pass filter parameter a = 5.0 and calculated with smoothing width W = 0.8.

Figure S5. P-wave velocity (!) and S-wave velocity (") by depth profiles at each station of the Oldest-1 array. Solid lines indicate median probability velocity profiles and 5 shaded background show the probability density function by depth. The station map is in Figure S6.

Figure S6. Map showing Oldest-1 array stations. Location of the nearest drilling site is marked with a red square and the stations are marked with orange circles.

Figure S7. Results of S6N09 inversion using shorter time spans, 1-year (2019.01–12), 6- months (2019.07–12), and 3-months (2019.07–09). The result of 5-year-long data is identical to Figure 10 in the main text. Input (a) R-stack, (b) R-ACF, and (c) Z-ACF waveforms of different time spans. (d, f, h) P-wave velocity probability density functions from inversions of 1-year, 6-month, and 3-month, overlain by the ! median probability profile from the 5-year inversion. (e, g, i) P-wave velocity probability density functions from inversions of 1- 6 year, 6-month, and 3-month, overlain by the !/" median probability profile from the 5-year inversion.

Figure S8. A schematic cartoon showing the rays considered in Figure 11b. The direction of the arrow points to the direction of the propagation; dark blue lines and light orange lines mark the propagating P wave and S wave, respectively. The top light blue layer is the water layer, the dark brown layer in the middle is the sediment layer, and the dark gray layer in the bottom is the crust layer.

Figure S9. Predicted Rayleigh-wave ellipticity (i.e., radial to vertical ratio) of the fundamental mode Rayleigh-wave using the sediment models of Bell *et al.* (2015) and this study. The crust and upper mantle layers in Bell *et al.* (2015) are added below the sediment model of this study for the computation. The difference between two predictions in frequencies above 0.10 Hz indicate that sediment models which had 7 general agreement in Rayleigh-wave admittance can be resolved using the Rayleigh-wave ellipticity.

Table S1. List of ocean bottom seismometer arrays used in this study. Arrays obtained from the IRIS MetaData Aggregator have network codes in parentheses. Studies with available seafloor sediment models around the stations and the country of origin of the instrumentation is specified on the right side of the table.

Table S2. List of frequency contents used in the analysis of ocean bottom seismometers.

Table S3. Numbers of teleseismic event waveforms stacked for the shorter operation period analysis with station S6N09 (Figure S7).

Table S4. Physical parameters of the layers used for calculating the expected amplification due to S transmission coefficients. The S-wave velocity of the sediment varies following the x-axis of Figure 11a. The slowness used for the calculation is 6.0×10^{-5} s/m.

Table S5. The model used for calculating transmission coefficients in Figure 11b. The slowness used for the coefficient calculation is 6.5×10^{-5} s/m.

Table S6. Crust and mantle layers added to the sediment model to compute Rayleigh wave predictions in Figures 12 and S8. For models from this study, we replaced the Upper Crust density and velocities using half-space crust layer density and velocities from

the inversion. These layered are assumed during the Rayleigh wave admittance inversion in Ruan *et al.* (2014) and Bell *et al.* (2015).

Please note: Oxford University Press is not responsible for the content or functionality of any supporting materials supplied by the authors. Any queries (other than missing material) should be directed to the corresponding author for the paper.

DATA AVAILABILITY

The OBS data from the Oldest-1 and Ontong Java Plateau arrays used in this study is available from the OHPDMC (Ocean Hemisphere Project Data Management Center 1997; http://ohpdmc. eri.u-tokyo.ac.jp/dataset/campaign/obs/index.html). The OBS data from other arrays are obtained from the IRIS DMC (http://service.iris.edu/fdsnws/dataselect/1/) with network codes Z6, YS and 7D (IRIS OBSIP 2011). The S-net data is available from the National Research Institute for Earth Science & Disaster Resilience (2019) upon registration on http://www.hinet.bosai.go.jp. The computer programme used in the study (REIN; reverberation waveform inversion) is available from zenodo (https://doi.org/10.5281/zenodo.10993545) or GitHub repository (https://github.com/seis-hyejeong/rein.git). Models from this study are available from zenodo (https://doi.org/10.5281/zenodo.10993278).

REFERENCES

Akaike, H., 1974. A new look at the statistical model identification, *IEEE Trans. Autom. Control,* **19**(6), 716–723.

Akuhara, T., Nakahigashi, K., Shinohara, M., Yamada, T., Shiobara, H., Yamashita, Y., Mochizuki, K. & Uehira, K., 2021. Lithosphere–asthenosphere boundary beneath the Sea of Japan from transdimensional inversion of S-receiver functions, *Earth Planets Space,* **73**(1), 171, doi:10.1186/s40623-021-01501-5

Barruol, G. *et al.* 2019. Large-scale flow of Indian Ocean asthenosphere driven by Réunion plume, *Nat. Geosci.,* **12,** 1043–1049.

Bell, S.W., Ruan, Y. & Forsyth, D.W., 2015. Shear velocity structure of abyssal plain sediments in Cascadia, *Seismol. Res. Lett.,* **86**(5), 1247–1252.

Brocher, T.M., 2005. Empirical relations between elastic wavespeeds and density in the earth's crust, *Bull. seism. Soc. Am.,* **95**(6), 2081–2092.

Castagna, J.P., Batzle, M.L. & Eastwood, R.L. 1985. Relationship between compressional-wave and shear-wave velocities in clastic silicate rocks, *Geophysics,* **50,** 571–581.

Chen, K.-X., Forsyth, D.W. & Fischer, K.M.(2024). A mid-lithospheric discontinuity detected beneath 155 ma western Pacific seafloor using Sp receiver functions, *Geophys. Res. Lett.,* **51,** e2024GL108347, doi:10.1029/2024GL108347

Chichester, B., Rychert, C., Harmon, N., Allen, R., Collier, J., Henstock, T. & Rietbrock, A., 2020. Seafloor sediment thickness beneath the VoiLA broad-band ocean-bottom seismometer deployment in the Lesser Antilles from P-to-S delay times, *Geophys. J. Int.,* **223**(3), 1758–1768,

Dai, Y., Rychert, C.A. & Harmon, N., 2023. Seismic imaging beneath Cascadia shows shallow mantle flow patterns guide lower mantle upwellings, *J. Geophys. Res.: Solid Earth,* **128,** e2023JB026374, doi:10.1029/2023JB026374

Doran, A.K. & Laske, G., 2019. Seismic structure of marine sediments and upper oceanic crust surrounding Hawaii, *J. Geophys. Res.: Solid Earth,* **124,** 2038–2056.

Eilon, Z., Abers, G.A., Jin, G. & Gaherty, J.B., 2014. Anisotropy beneath a highly extended continental rift, *Geochem. Geophys. Geosyst.,* **15,** 545–564.

Eilon, Z.C., Zhang, L., Gaherty, J.B., Forsyth, D.W. & Russell, J.B., 2022. Sub-lithospheric small-scale convection tomographically imaged beneath the Pacific plate, *Geophys. Res. Lett.,* **49,** e2022GL100351, doi:10.1029/2022GL100351

Fujie, G., Kodaira, S., Yamashita, M., Sato, T., Takahashi, T. & Takahashi, N., 2013. Systematic changes in the incoming plate structure at the Kuril trench, *Geophys. Res. Lett.,* **40**, 88–93..

Hamilton, E.L.(1979). Vp/Vs and Poisson's ratios in marine sediments and rocks, *J. Acoust. Soc. Am.,* **66**(4), 1093–1101.

Hannemann, K., Krüger, F., Dahm, T. & Lange, D. 2016. Oceanic lithospheric S-wave velocities from the analysis of P-wave polarization at the ocean floor, *Geophys. J. Int.,* **207**(3), 1796–1817.

IRIS OBSIP, 2011. Cascadia Initiative Community Experiment—OBS Component. International Federation of Digital Seismograph Networks.

Isse, T. *et al.* 2021. Seismic evidence for a thermochemical mantle plume underplating the lithosphere of the Ontong Java Plateau, *Commun. Earth Environ.,* **2**, 98, doi:10.1038/s43247-021-00169-9

Janiszewski, H.A., Eilon, Z., Russell, J.B., Brunsvik, B., Gaherty, J.B., Mosher, S.G., Hawley, W.B. & Coats, S., 2023. Broad-band ocean bottom seismometer noise properties, *Geophys. J. Int.,* **233**(1), 297–315.

Kang, H. *et al.* 2023. Seismic velocity structure of upper mantle beneath the oldest Pacific seafloor: insights from finite-frequency tomography, *Geochem. Geophys. Geosyst.,* **24**, e2022GC010833, doi:10.1029/2022GC010833

Kawakatsu, H. & Utada, H., 2017. Seismic and electrical signatures of the lithosphere-asthenosphere system of the normal Oceanic mantle, *Annu. Rev. Earth Planet. Sci.,* **45**, 139–167.

Kawakatsu, H., Kumar, P., Takei, Y., Shinohara, M., Kanazawa, T., Araki, E. & Suyehiro, K., 2009. Seismic evidence for sharp lithosphere-asthenosphere boundaries of oceanic plates, *Science,* **324**, 499–502.

Kawano, Y. *et al.* 2023. Seismic structure of the lithosphere-asthenosphere system beneath the oldest seafloor revealed by Rayleigh-wave dispersion analysis, *J. Geophys. Res.: Solid Earth,* **128**, e2023JB026529, doi:10.1029/2023JB026529

Kim, HJ., Kawakatsu, H., Akuhara, T. & Takeuchi, N., 2023. Characterizing the seafloor sediment layer using teleseismic body waves recorded by ocean bottom seismometers, *J. Geophys. Res.: Solid Earth,* **128**, e2023JB027616, doi:10.1029/2023JB027616

Kim, HJ., Kawakatsu, H., Akuhara, T., Shinohara, M., Shiobara, H., Sugioka, H. & Takagi, R., 2021. Receiver function imaging of the amphibious NE Japan subduction zone—Effects of low-velocity sediment layer, *J. Geophys. Res.: Solid Earth,* **126**, e2021JB021918, doi:10.1029/2021JB021918

Koppers, A.A., Staudigel, H., Pringle, M.S. & Wijbrans, J.R., 2003. Short-lived and discontinuous intraplate volcanism in the South Pacific: hot spots or extensional volcanism?, *Geochem. Geophys. Geosyst.,* **4**(10), doi:10.1029/2003GC000533

Lancelot, Y.P. *et al.* 1990. *Site 802. Proceedings of the Ocean Drilling Program, Part A: Initial Reports,* College Station, TX (Ocean Drilling Program)., Vol., **129**, pp. 171–243.

Laske, G., Masters., G., Ma, Z. & Pasyanos, M., 2013. Update on CRUST1.0–A 1-degree global model of Earth's crust, *Geophys. Res. Abstr.,* **15**, EGU2013–2658.

Mosher, S.G., Audet, P. & Gosselin, J.M., 2021. Shear-wave velocity structure of sediments on Cascadia's continental margin from probabilistic inversion of seafloor compliance data, *Geochem. Geophys. Geosyst.,* **22**, e2021GC009720, doi:10.1029/2021GC009720

Nakamura, Y. *et al.* 2014. Seismic imaging and velocity structure around the JFAST drill site in the Japan Trench: low vp, high vp/vs in the transparent frontal prism, *Earth Planets Space,* **66**, 121, doi:10.1186/1880-5981-66-121

National Research Institute for Earth Science and Disaster Resilience, 2019. *NIED S-net*. National Research Institute for Earth Science and Disaster Resilience.

Obayashi, M. *et al.* 2021. Interrelation of the stagnant slab, Ontong Java Plateau, and intraplate volcanism as inferred from seismic tomography, *Sci. Rep.,* **11**, 20 966, doi:10.1038/s41598-021-99833-5

Obayashi, M., Ishihara, Y. & Suetsugu, D., 2017. Effects of shallow-layer reverberation on measurement of teleseismic p-wave travel times for ocean bottom seismograph data, *Earth Planets Space,* **69**(1), 44, doi:10.1186/s40623-017-0626-2

Ocean Hemisphere Project Data Management Center, 1997. Data obtained by the ocean hemisphere project. Retrieved from http://ohpdmc.eri.u-tokyo.ac.jp Last Accessed 2024 September 20

Premoli Silva, I. *et al.* 1993. *Site 878. Proc. Ocean Drilling Program, Part A: Initial Reports,* College Station, TX (Ocean Drilling Program), Vol., **144**, pp. 331–412.

Ruan, Y., Forsyth, D.W. & Bell, S.W., 2014. Marine sediment shear velocity structure from the ratio of displacement to pressure of Rayleigh waves at seafloor, *J. Geophys. Res.: Solid Earth,* **119**(8), 6357–6371.

Russell, J.B. & Dalton, C.A., 2022. Rayleigh wave attenuation and amplification measured at ocean-bottom seismometer arrays using Helmholtz tomography, *J. Geophys. Res.: Solid Earth,* **127**, e2022JB025174, doi:10.1029/2022JB025174

Rychert, C.A., Harmon, N. & Tharimena, S., 2018. Scattered wave imaging of the oceanic plate in Cascadia, *Sci. Adv.,* **4**(2), eaao1908, doi:10.1126/sciadv.aao1908

Saikia, U., Rychert, C., Harmon, N. & Kendall, J.M., 2020. Sediment structure at the equatorial mid-Atlantic ridge constrained by seafloor admittance using data from the pi-lab experiment, *Mar. Geophys. Res.,* **41**(1), 3, doi:10.1007/s11001-020-09402-0

Saikia, U., Rychert, C.A., Harmon, N. & Michael Kendall, J., 2021. Seismic attenuation at the equatorial Mid-Atlantic Ridge constrained by local Rayleigh wave analysis from the PI-LAB experiment, *Geochem. Geophys. Geosyst.,* **22**, e2021GC010085, doi:10.1029/2021GC010085

Sambridge, M., 2014. A Parallel Tempering algorithm for probabilistic sampling and multimodal optimization, *Geophys. J. Int.,* **196**(1), 357–374.

Schlömer, A., Geissler, W.H., Jokat, W. & Jegen, M., 2017. Hunting for the Tristan mantle plume—An upper mantle tomography around the volcanic island of Tristan da Cunha, *Earth Planet. Sci. Lett.,* **462**, 122–131.

Shinohara, M. *et al.* 2008. Upper mantle and crustal seismic structure beneath the Northwestern Pacific Basin using a seafloor borehole broadband seismometer and ocean bottom seismometers, *Phys. Earth Planet. Inter.,* **170**(1–2), 95–106.

Straume, E.O., Gaina, C., Medvedev, S., Hochmuth, K., Gohl, K., Whittaker, J.M. & Hopper, J.R., 2019. Globsed: updated total sediment thickness in the world's oceans, *Geochem. Geophys. Geosyst.,* **20**(4), 1756–1772.

Suetsugu, D. & Shiobara, H., 2014. Broadband ocean-bottom seismology, *Annu. Rev. Earth Planet. Sci.,* **42**, 27–43.

Takagi, R., Toyokuni, G. & Chikasada, N., 2020. Ambient noise correlation analysis of S-net records: extracting surface wave signals below instrument noise levels, *Geophys. J. Int.,* **224**(3), 1640–1657.

Takeo, A., Kawakatsu, H., Isse, T., Nishida, K., Shiobara, H., Sugioka, H., Ito, A. & Utada, H., 2018. In situ characterization of the lithosphere-asthenosphere system beneath NW Pacific Ocean via broadband dispersion survey with two OBS arrays, *Geochem. Geophys. Geosyst.,* **19**, 3529–3539.

Takeuchi, N., Isse, T., Kawakatsu, H., Shiobara, H., Sugioka, H., Ito, A., Utada, H. & Yamada, T., 2023. Olivine fabrics in the oceanic lithosphere constrained by Pn azimuthal anisotropy, *J. Geophys. Res.: Solid Earth,* **128**, e2023JB026428, doi:10.1029/2023JB026428

Takeuchi, N., Kawakatsu, H., Shiobara, H., Isse, T., Sugioka, H., Ito, A. & Utada, H., 2017. Determination of intrinsic attenuation in the oceanic lithosphere-asthenosphere system, *Science,* **358**, 1593–1596.

Tonegawa, T., Miura, S., Ishikawa, A., Sano, T., Suetsugu, D., Isse, T. & Kobayashi, T., 2019. Characterization of crustal and uppermost mantle seismic discontinuities in the Ontong Java Plateau, *J. Geophys. Res.: Solid Earth,* **124**(7), 7155–7170.

Wessel, P., Smith, W.H.F., Scharroo, R., Luis, J & Wobbe, F., 2013. Generic mapping tools: improved version released, *Eos Trans. Am. Geophys. Union,* **94**(45), 409–410.

Yu, Y., Song, J., Liu, K.H. & Gao, S.S., 2015. Determining crustal structure beneath seismic stations overlying a low-velocity sedimentary layer using receiver functions, *J. Geophys. Res.: Solid Earth,* **120**, 3208–3218.